

AN INTEGRATED FRAMEWORK FOR LIGHT CURVE
SIMULATION AND SHAPE INVERSION OF HUMAN-MADE
SPACE OBJECTS

by

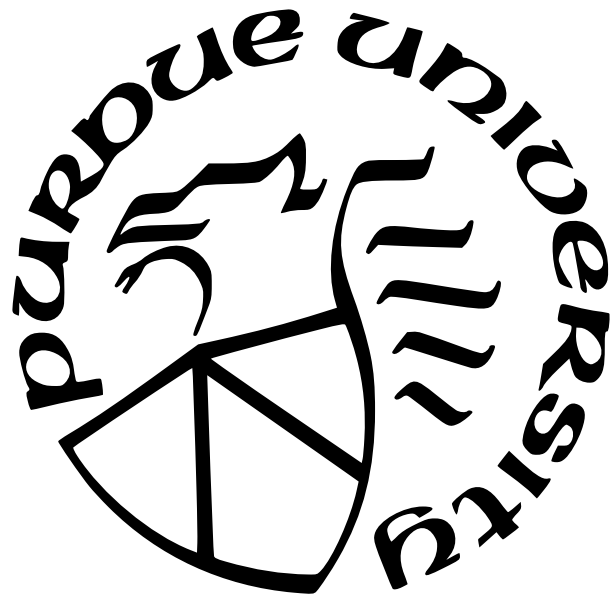
Liam Robinson

A Thesis

Submitted to the Faculty of Purdue University

In Partial Fulfillment of the Requirements for the degree of

Master of Science in Aeronautics and Astronautics



School of Aeronautics and Astronautics

West Lafayette, Indiana

December 2023

**THE PURDUE UNIVERSITY GRADUATE SCHOOL
STATEMENT OF COMMITTEE APPROVAL**

Dr. Carolin Frueh

School of Aeronautics and Astronautics

Dr. Kenshiro Oguri

School of Aeronautics and Astronautics

Dr. Keith LeGrand

School of Aeronautics and Astronautics

Approved by:

Dr. Carolin Frueh

ACKNOWLEDGMENTS

This work was supported by Katalyst grant number, Boeing grant number, and the National Defense Science and Engineering Graduate Fellowship through the Air Force Office of Scientific Research.

TABLE OF CONTENTS

LIST OF TABLES	7
LIST OF FIGURES	8
LIST OF LISTINGS	9
LIST OF SYMBOLS	10
ABSTRACT	11
1 Introduction	12
2 Literature	13
2.1 Coordinate Systems	16
2.1.1 International Terrestrial Reference Frame	16
2.1.2 Right Ascension and Declination	16
2.1.3 Azimuth and Elevation	16
2.2 Time Systems	17
3 MESHES	18
4 ATTITUDE REPRESENTATIONS	19
5 LIGHTING	22
5.1 The Bidirectional Reflectance Distribution Function	22
5.1.1 BRDF Formulations	23
Lambertian	23
Phong	24
Blinn-Phong	24
Glossy	24
6 Light Curves	26
6.1 Brightness Units	26

6.1.1	Irradiance	26
6.1.2	Normalized Irradiance	27
6.1.3	S_{10}	27
6.1.4	Magnitudes per Square Arcsecond	27
6.1.5	Candela	28
6.1.6	Photoelectron Counts	29
6.2	Astronomical Spectra	30
7	Background Signals	32
7.1	Atmospheric Effects	32
7.1.1	Airglow	32
7.1.2	Light Pollution	33
7.1.3	Twilight	34
7.2	Exoatmospheric Effects	36
7.2.1	Integrated Starlight	36
7.2.2	Scattered Moonlight	38
7.2.3	Zodiacal Light	41
7.2.4	Sampling Background	42
7.2.5	Background Source Importance	43
7.3	Sensor Effects	43
7.3.1	Dark Noise	43
7.3.2	Readout Noise	43
8	Light Curve Simulation	44
8.0.1	Simulating Convex Objects	44
9	Appendices	45
9.1	Astronomical Spectra Data	45
Atmospheric Extinction	45
Quantum Efficiency	45
9.1.1	Background Source Data	45

Lunar Phase Factor	45
Scattered Moonlight	46
Zodiacal Light	47
9.1.2 Telescope Parameters	47
Purdue Optical Ground Station	47
REFERENCES	49

LIST OF TABLES

7.1	Background signal importance	43
9.1	Purdue Optical Ground Station telescope parameters	48

LIST OF FIGURES

2.1	Time systems relative to TAI	17
5.1	Implemented BRDFs rendered with arbitrary parameters. Figure demonstrates the qualitative differences in each lighting model.	25
6.1	Luminous efficiency function from [36]	29
6.2	Astronomical Spectra	31
7.1	Mean airglow signal on the local observer hemisphere. The observer is in New Mexico, USA at 32.900° N, -105.533° W	33
7.2	Zenith light pollution in the eastern USA, data from [39]	34
7.3	Mean light pollution signal on the local observer hemisphere. The observer is in New Mexico, USA at 32.900° N, -105.533° W	35
7.4	Twilight model surface brightness at zenith as a function of solar zenith angle .	36
7.5	Mean twilight signal on the local observer hemisphere. The observer is in New Mexico, USA at 32.900° N, -105.533° W	37
7.6	Raw image of three GEO objects with stars streaking through the background. Taken by the Purdue Optical Ground station at 32.900° N, -105.533° W by Nathan Houtz	38
7.7	Integrated starlight patched catalog	39
7.8	Integrated starlight signal on the local observer hemisphere. The observer is in New Mexico, USA at 32.900° N, -105.533° W	40
7.9	Mean scattered moonlight signal on the local observer hemisphere. The observer is in New Mexico, USA at 32.900° N, -105.533° W	41
7.10	Mean zodiacal light signal on the local observer hemisphere. The observer is in New Mexico, USA at 32.900° N, -105.533° W	42

LIST OF LISTINGS

LIST OF SYMBOLS

I irradiance in $\left[\frac{W}{m^2}\right]$

\hat{I} normalized irradiance in $[W]$

ABSTRACT

PurdueThesis is a L^AT_EX document class used for master's bypass reports, master's theses, PhD dissertations, and PhD preliminary reports. This template demonstrates how to use PurdueThesis.

1. Introduction

This is the introduction

2. Literature

Light curve simulation methods differ between approaches and the object class under study. Kaasalainen and Torppa employ a Lambertian model for convex objects with a facetwise ray tracing scheme for non-convex objects [1]. Fan, Friedman, Kobayashi, and Frueh [2]–[6] use a nearly identical scheme for human-made objects. Allworth et al. developed a ray traced simulator for light curves in Blender, accounting for photorealistic shadowing and motion blur [7], [8]. Many deep learning approaches including Furfaro et al. [9] and Cabrera and Bradley [10], [11] use a simple Lambertian model with no self-shadowing. Linares and Crassidis [12] apply a more specialized approach with a non-Lambertian Bidirectional Reflectance Distribution Function (BRDF) for lighting. McNally et al. [13] use a Phong BRDF without shadowing shadowing, citing computational intensity. Blacketer [14] implemented a Cook-Torrance BRDF for lighting with a plane stacking method for self-shadowing.

Methods for shape inversion fall into three major categories: Extended Gaussian Image (EGI), statistical estimation, and deep learning based methods, each approaching the problem from a different perspective.

Direct light curve inversion with the EGI uses a series of optimization problems to fit a convex shape to measurements. These methods were pioneered by Kaasalainen and Torppa for asteroids in [1] with simultaneous attitude inversion in [1]. While natural space objects like asteroids are largely convex, nearly all human-made space objects are highly non-convex, highlighting the need for a robust inversion scheme for both convex and non-convex space objects. The work of Kaasalainen et al. on asteroids was extended by Chng et al. [15] to find globally optimal spin pole and area vector solutions. Calef et al. [16] were early adopters of Kaasalainen and Torppa’s EGI methods for human-made objects, focusing on multispectrum measurements. Bradley and Axelrad [11] applied EGI methods to recover convex approximations of representative GEO objects. Fan and Frueh [3], [17], [18] used the EGI with a multi-hypothesis scheme to recover human-made object shapes with measurement noise. Friedman [4], [19] quantified the observability of EGI inversion to inform sensor tasking schemes. Cabrera et al. [10] studied the effects of area regularization on Fan and Friedman’s methods to achieve more accurate reconstructions.

A second approach leverages statistical estimation to retrieve shape information. Linares et al. [20] applied an unscented Kalman filter to estimate attitude and convex shape simultaneously, representing shape with vertex displacement on a sphere. Linares et al. [21] used a Multiple-Model Adaptive Estimation (MMAE) algorithm to predict the truth geometry and attitude by comparing observations with a bank of reference objects. Linares and Crassidis [12] used an an Adaptive Hamiltonian Markov Chain Monte Carlo scheme to estimate shape and other characteristics simultaneously.

A third approach relies on deep learning. Linares and Furfaro [22] used a deep convolutional neural network to classify novel light curves as rocket bodies, payloads, or debris. Furfaro et al. [9] used similar methods classify novel light curves into four truth object classes. Kerr et al. [23] adapted the architecture developed by Furfaro et al. to classify object shape and size in an extended training set. McNally et al. [13] use AI and differential approaches to identify satellites from simulated and real light curves. Allworth et al. [8] applied transfer learning to simulated and real measurements to classify object type.

Various other unique methods have been applied to the light curve shape inversion problem. Hall et al. [24] investigated methods for independently solving shape parameters in isolation without attitude information. Fulcoly et al. [25] used measurements from different sensor locations to determine shape under various attitude profiles. Yanagisawa and Kurosaki [26] fit an analytical light curve model for a tri-axial ellipsoid to derive the shape and attitude profile of a Cosmos rocket body. Kobayashi applied compressed sensing to recover shape information from light curves by taking advantage of shadowing geometry [5], [27].

Shape inversion for non-convex objects — mainly asteroids — has been studied by others in the past. Durech and Kaasalainen [28] determined a relationship between concavity size and the minimum solar phase angle where self-shadowing impacts the light curve. Viikinkoski et al. [29] investigated recovering large concavities from adaptive optics imagery, noting the fundamental non-uniqueness of any solution. They discuss how a single large concavity may produce identical scattering behavior to multiple smaller concave features [29]. Cabrera et al. [10] studied convex solutions for non-convex objects, concluding that the convex fit diverges from the true shape as the relative concavity size increases.

We approach the shape inversion problem with the foundational EGI optimization and object reconstruction methods of [1], [3]. The EGI optimization processes of [1], [3], [10] are improved using novel resampling and merging steps. These improvements circumvent the need for the regularization terms explored by Cabrera et al. [10]. We also address the reconstruction scaling issues present in Fan’s work [3] with an objective function proposed by Ikeuchi et al. [30] in place of Little’s [31]. The support optimization procedure is accelerated and strengthened with a preconditioning term proposed by Nicolet et al. [32], enabling the rapid reconstruction of more detailed convex objects than previously feasible.

Our approach has a number of general advantages. We do not require any *a priori* information about the truth geometry. Thus, unlike MMAE methods [21], we do not require a bank of reference models to recover shape information. Unlike deep learning methods, our method does not rely on the diversity of a training set to achieve realistic results [9], [23]. Our light curve simulation method improves on the facetwise ray traced shadows of [1], [3], [6] with shadow mapping, increasing shadow fidelity per unit computation time.

2.1 Coordinate Systems

2.1.1 International Terrestrial Reference Frame

The most intuitive Earth-centered reference frame is Earth-centered Earth-fixed (ECEF). An ECEF frame has its origin at the center of mass of the Earth and its axes fixed in the crust. The fundamental plane of the frame is defined to be the equator — defining the z -axis through Earth's instantaneous spin axis, and the reference direction through the intersection of the prime meridian and the equator — defining the x -axis. Completing the right-handed system the y -axis yields a reference frame that remains fixed, neglecting continental drift and other pesky (but sufficiently negligible) realities.

2.1.2 Right Ascension and Declination

Right ascension and declination, often shortened to RA/Dec, are useful angles from describing the angular position of an object on the celestial sphere from the perspective of an observer. Right ascension is defined as the angle of the observation projected onto the inertial $x - y$ plane, measured counterclockwise from inertial \hat{x} , represented by α . Declination is the angle from the $x - y$ plane to the observation with positive values above the $x - y$ plane (closer to inertial z) and negative values below. Declination is represented by δ . Given a unit vector direction $\hat{v} = [x, y, z]^T$ in inertial space, we can compute RA/Dec via Eq 2.1.

$$\begin{bmatrix} \alpha \\ \delta \end{bmatrix} = \begin{bmatrix} \text{atan2}(y, x) \\ \text{atan2}(z, \sqrt{(x^2 + y^2)}) \end{bmatrix} \quad (2.1)$$

2.1.3 Azimuth and Elevation

Azimuth and elevation, often shortened to Az/El, are similar angular quantities to right ascension and declination, but instead of being based on the inertial sphere, they are referenced to an arbitrary reference frame. For a telescope making observations of an object, the local East-North-Up (ENU) frame may be used. For a satellite star tracker, star azimuth

and elevation might be reported in the satellite body frame. In either case, Eq 2.1 can be repurposed in terms of Az/El, where $\hat{v} = [x, y, z]^T$ is expressed in the frame of interest.

$$\begin{bmatrix} Az \\ El \end{bmatrix} = \begin{bmatrix} \text{atan2}(y, x) \\ \text{atan2}(z, \sqrt{(x^2 + y^2)}) \end{bmatrix} \quad (2.2)$$

Note that Eq 2.2 references azimuth to the x -axis, proceeding in the counterclockwise direction. Often, this reference axis and direction may be changed depending on the reference frame being used. For example, ground station observations may be referenced to local North — the second axis of the ENU system — proceeding clockwise. This would require the substitution $Az' = \frac{\pi}{2} - Az$. Notice that this substitution leads to Az' leaking outside the domain of $[0, 2\pi]$. This is not an issue for later coordinate transformations, but may be undesirable for plots. Wrapping the result back to the standard azimuth range via $Az_{wrapped} = \text{mod}(Az, 2\pi)$ is a sufficient fix.

2.2 Time Systems

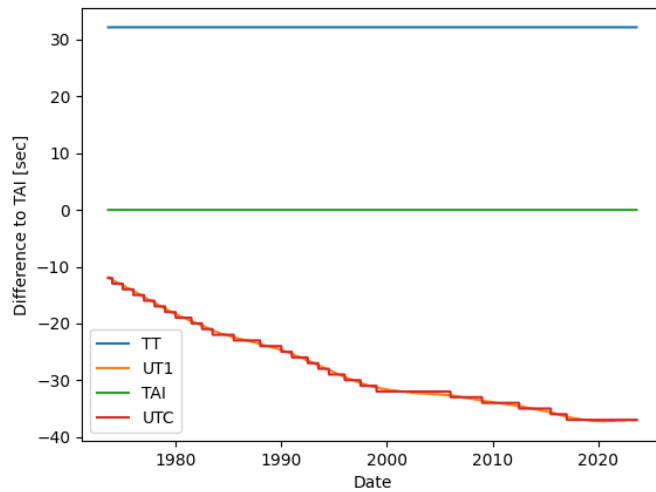


Figure 2.1. Time systems relative to TAI

3. MESHES

A computer represents 3D objects

4. ATTITUDE REPRESENTATIONS

When we talk about the orientation — also known as attitude — of a rigid body in three dimensions, that orientation is always implicitly understood to be relative to some other reference frame. The orientation of a book might be expressed using a frame fixed in the table it sits on. If that same book was sitting in an empty void, we would have no way to talk — or even think — about its orientation. Orientation itself is a three-dimensional quantity. Consider a coordinate system fixed in a rigid object and a second reference frame in which we want to express the orientation of the object. For convenience, we will call the frame fixed in the object the body frame, and the second frame the world frame. Any effective attitude representation must let us express the directions of all three body axes in terms of the world frame basis vectors. This raises an important question: how many numbers do we need to express an object's attitude? We can express the direction of any unit vector with two numbers — the azimuth and elevation of that vector. Naïvely, we might extrapolate from this to conclude that we will need six numbers to express an orientation. Because the basis vectors form an orthonormal set $\{\hat{b}_1, \hat{b}_2, \hat{b}_3\}$, we know we can express $\hat{b}_3 = \hat{b}_1 \times \hat{b}_2$, $\hat{b}_2 = \hat{b}_3 \times \hat{b}_1$, and $\hat{b}_1 = \hat{b}_2 \times \hat{b}_3$. Each of these equations constrains one further degree of freedom, indicating that only three quantities are necessary to express the relative orientation of two reference frames. The most obvious parameterization for attitude is the direction cosine matrix (DCM), a 3×3 symmetric matrix with determinant 1. We notate the DCM with two capital letters, the rightmost indicating the reference frame of the input vectors and the leftmost indicating the transformed frame. Alternatively, the DCM is sometimes expressed as C when the frames involved are arbitrary or do not need to be denoted. For example, the DCM $[\mathcal{B}\mathcal{N}]$ takes vectors in the \mathcal{N} frame to the \mathcal{B} frame:

$${}^{\mathcal{B}}\mathbf{r} = [\mathcal{B}\mathcal{N}]^{\mathcal{N}}\mathbf{r} \quad (4.1)$$

The orthogonal property of the DCM implies $[\mathcal{B}\mathcal{N}]^{-1} = [\mathcal{B}\mathcal{N}]^T$ such that $[\mathcal{B}\mathcal{N}]^T = [\mathcal{N}\mathcal{B}]$.

Another core attitude representation is the Euler angle-axis form. Euler's rotation theorem guarantees that any relative orientation can be expressed as a single rotation about an axis $\hat{\lambda} \in \mathbb{S}^2$ by an angle $\theta \in [0, 2\pi]$. The set $\{\hat{\lambda}, \theta\}$ is known as a principal rotation

parameter, abbreviated PRP hereafter. The DCM is mapped to the PRP representation via [33]

$$\theta = \cos^{-1} \left(\frac{1}{2} [C_{1,1} + C_{2,2} + C_{3,3} - 1] \right) \quad (4.2)$$

$$\hat{\lambda} = \frac{1}{2 \sin \theta} \begin{bmatrix} C_{2,3} - C_{3,2} \\ C_{3,1} - C_{1,3} \\ C_{1,2} - C_{2,1} \end{bmatrix} \quad (4.3)$$

Where $C_{i,j}$ refers to the i th row and j th column of C . The mapping from PRP to DCM is also relatively straightforward:

$$C = I_3 + \sin \theta [\hat{\lambda} \times] + (1 - \cos \theta) [\hat{\lambda} \times]^2 \quad (4.4)$$

Where $[v \times]$ is the matrix cross product operator, defined on $\mathbf{v} \in \mathbb{R}^3$ as:

$$[\mathbf{v} \times] = \begin{bmatrix} 0 & -v_3 & v_2 \\ v_3 & 0 & -v_1 \\ -v_2 & v_1 & 0 \end{bmatrix} \quad (4.5)$$

This operator is useful in that it takes care of cross products for us, i.e. $\mathbf{v} \times \mathbf{u} = [\mathbf{v} \times] \mathbf{u}$. While the PRP $\{\theta, \hat{\lambda}\}$ is a four element set, there are only three degrees of freedom due to the unit norm constraint on $\hat{\lambda}$. This means that we can multiply the Euler angle by the axis, yielding a closely related attitude representation known as the rotation vector (RV), generally denoted \mathbf{p} .

$$\mathbf{p} = \theta \hat{\lambda} \quad (4.6)$$

The RV is the first truly three dimensional representation we have come across so far. This is advantageous for visualizing sets of orientations, but there are multiple notable issues with any three dimensional embedding of $SO(3)$. Any representation embedded in \mathbb{R}^3 loses

	DCM	PRP	RV	MRP
DCM	—			
PRP	$C = I_3 + \sin \theta [\hat{\lambda} \times] + (1 - \cos \theta) [\hat{\lambda} \times]^2$	—	$\mathbf{p} = \theta \hat{\lambda}$	
RV			—	
MRP				—

some of the spherical qualities of \mathbb{S}^3 , leading to singularities — regions where attitudes are not uniquely defined or are impossible to compute in the first place.

To summarize, we can transform to and from all attitude representations with relatively simple algebraic operations:

5. LIGHTING

5.1 The Bidirectional Reflectance Distribution Function

Although light curves come from unresolved measurements, the interactions that produce them are directly driven by the shape and material properties of the object being observed. In order to simulate accurate light curves, we must model all important optical interactions. In broad terms, this boils down to determining how the object is lit and how it is shadowed.

At the microscopic scale, the surface of an object is composed of facets — small areas sharing a normal vector. The macroscopic optical properties of the material is driven by the distribution of sizes and normal directions of the facets. If the facets are distributed in biased orientations, the macroscopic surface may show anisotropy, leading to the appearance of brushed metal. If the facets normals are at large angles to each other, the surface may appear dull as the outgoing direction of the light may be completely independent from the incoming direction. Subsurface effects — where incoming light rays scatter *inside* the surface can also change the macroscopic properties of the material.

This discussion raises an important question; how can we model the macroscopic outcomes of the true microscopic interactions of incident light on a surface? The bidirectional reflectance distribution function (BRDF) is a tool developed in computer graphics to address this exact problem. The BRDF is a function on the hemisphere which expresses the fraction of light per solid angle (radiance \mathcal{R}) leaving the surface in a given direction, divided by the incident power per unit area (irradiance \mathcal{I}). The general formulation for a BRDF f_r is given by Eq 5.1 [34].

$$f_r(\mathbf{x}, L \rightarrow O) = \frac{d\mathcal{R}(\mathbf{x} \rightarrow O)}{d\mathcal{I}(L \rightarrow \mathbf{x})}. \quad (5.1)$$

In Eq 5.1, $\mathbf{x} \in \mathbb{R}^3$ is the point on the object's surface the BRDF is evaluated at. $L \in \mathbb{S}^2$ is the incoming illumination unit vector and $O \in \mathbb{S}^2$ is the outgoing unit vector. Note that this work treats $f_r(\mathbf{x}, L \rightarrow O)$ and $f_r(L \rightarrow O)$ as equivalent in later descriptions, leaving the evaluation point \mathbf{x} implied. This definition is useful for building intuition about the form of the BRDF, but to represent a physically plausible reflection process, a candidate function

must satisfy three additional constraints. A physically plausible BRDF must conserve energy — more energy cannot leave the surface than was incident on it, neglective thermal effects. It must also be reciprocal — switching the observer and illumination directions should not change the BRDF value as the surface interaction. This reciprocity is sometimes known as the *Helmholtz Reciprocity Rule* in literature [montes2012](#). Finally, plausible BRDFs must take on nonnegative values for all inputs [montes2012](#). A surface cannot reflect negative light, so this should feel natural. Explicitly, energy conservation is expressed by Eq 5.2 [montes2012](#).

$$\forall L \in \Omega : \int_{O \in \Omega} f_r(L \rightarrow O) d\Omega \leq 1 \quad (5.2)$$

Eq 5.2 states that for all possible illumination directions L on the hemisphere Ω you can integrate all possible outgoing observer directions O on the hemisphere and end up with equal or less energy than you started with. Reciprocity can also be formalized via 5.3.

$$\forall L, O \in \Omega : f_r(L \rightarrow O) = f_r(O \rightarrow L) \quad (5.3)$$

5.1.1 BRDF Formulations

The following BRDFs are all energy conserving, reciprocal, and nonnegative. *Caveat emptor:* this does not mean that they are always sufficient for modeling real-world materials, they merely represent ways hypothetical surfaces could reflect light without breaking any fundamental physics.

Lambertian

The simplest BRDF is one that reflects equally in all directions. This BRDF is termed Lambertian or diffuse.

$$f_r(L \rightarrow O) = \frac{C_d}{\pi} \quad (5.4)$$

In Eq 5.4, $0 \leq C_d \leq 1$ is the surface's coefficient of diffuse reflection. If $C_d = 0.4$, we know that the surface reflects 40% of incident radiation and absorbs the other 60%.

Phong

A simple specular BRDF model is that developed by Phong in 1975 **phong1975**. The Phong model splits the BRDF into a Lambertian term governed by C_d and a specular term governed the coefficient of specular reflection $0 \leq C_s \leq 1$ and the specular exponent $n \geq 0$ [34].

$$f_r(L \rightarrow O) = \frac{C_d}{\pi} + \frac{C_s \frac{n+2}{2\pi} (O \cdot R)^n}{N \cdot L} \quad (5.5)$$

In Eq 5.5, R is the reflected illumination vector, computed via $R = 2(N \cdot L)N - L$. As n increases, the specular glint becomes sharper and more intense, eventually approaching a perfectly mirror reflection. Now that we have two coefficients of reflection, we must add an new constraint to maintain energy conservation. Because C_d and C_s each represent the *fraction* of light reflected in each mode, it should be clear that $C_d + C_s \leq 1$. This can also be reformulated with an explicit coefficient of absorption C_a which captures the fraction of incident radiation absorbed by the surface, yielding $C_d + C_s + C_a = 1$.

Blinn-Phong

The Blinn-Phong BRDF is similar to the Phong BRDF, but parameterizes the specular lobe in terms of the halfway vector H [34]. This vector is halfway between the illumination and observer directions such that $H = L + O$ which needs to be normalized before use. As the halfway vector approaches the surface normal vector, the observer must be approaching the reflected illumination vector, leading to a more intense specular highlight.

$$f_r(L \rightarrow O) = \frac{C_d}{\pi} + \frac{C_s \frac{n+2}{2\pi} (N \cdot H)^n}{4(N \cdot L)(N \cdot O)} \quad (5.6)$$

Glossy

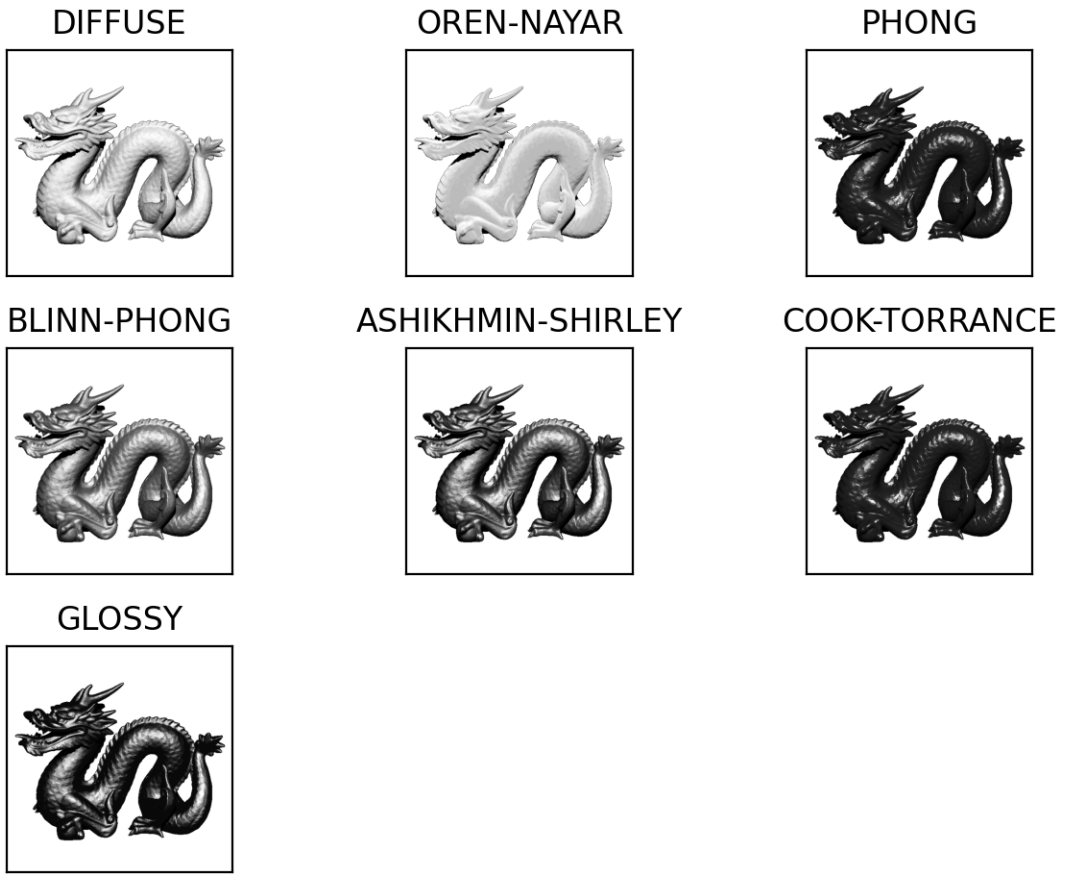


Figure 5.1. Implemented BRDFs rendered with arbitrary parameters. Figure demonstrates the qualitative differences in each lighting model.

6. Light Curves

A light curve is a time series of unresolved optical brightness measurements. Once an object is far enough away from the observer to become unresolved, all geometric data is lost and the only information that remains in the individual measurements is the total brightness. "Brightness" is a catch-all term for a variety of units.

6.1 Brightness Units

6.1.1 Irradiance

Irradiance is the standard SI linear unit used to describe the total amount of energy incident on a surface from a given source. An irradiance of $1 \left[\frac{W}{m^2} \right]$ implies that a $10 [m]$ area would experience $10 [W]$ of incident power. The Sun's irradiance is approximately $1361 \left[\frac{W}{m^2} \right]$ at a distance of 1 AU.

Visual magnitude — also known as apparent or relative magnitude — is a reverse logarithmic scale that originates in astronomy. Stellar sources span many orders of magnitude of brightness, making a logarithmic scale a helpful middle ground for comparison. Note that apparent magnitude always expresses brightness at the observer's location; absolute magnitude is a different quantity that normalizes brightness from a distance of 10 parsecs. In terms of irradiance, apparent magnitude is computed via Eq 6.1.

$$m = -2.5 \log_{10} \left(\frac{I}{I_0} \right) \quad (6.1)$$

In Eq 6.1, I is the irradiance of the source of interest and I_0 is irradiance of the zero-point source. This makes sense as if we plug in $I = I_0$, we are left with $m = 0$. The star Vega is usually taken to be the zero-point with irradiance $I_0 = 2.518021002 \cdot 10^{-8} \left[\frac{W}{m^2} \right]$.

We can rearrange Eq 6.1 to compute irradiance from a given apparent magnitude, yielding Eq 6.2

$$I = I_0 \cdot 10^{-\frac{m}{2.5}} \quad (6.2)$$

6.1.2 Normalized Irradiance

This work also uses normalized irradiance, the irradiance of a source if the observer was 1 meter away. This is a non-standard quantity in the literature, but proves useful for the same reasons absolute magnitude is used by astronomers. Adjusting sources to be at a standard distance allows us to simulate and invert light curves in a non-dimensionalized space, simplifying simulation and making the inversion optimizations more robust. To make the conversion explicit, irradiance observed at a distance r in meters from an object is converted to normalized irradiance \hat{I} in Watts via Eq 6.3

$$\hat{I} = r^2 I \quad (6.3)$$

6.1.3 S_{10}

While magnitude and irradiance do a good job describing the flux of point sources, other units exist to talk about diffuse or extended sources where brightness is somewhat uniformly spread over an area. S_{10} is a unit of surface brightness represented by the number of 10th magnitude stars per square degree that would produce the same flux. Surface brightness in S_{10} over a given solid angle Ω [rad^2] can be converted to total irradiance I [$\frac{\text{W}}{\text{m}^2}$] via Eq 6.4.

$$\frac{I \left[\frac{\text{W}}{\text{m}^2} \right]}{S_{10}} = 10^{-10/2.5} \left(\Omega \frac{180^2}{\pi^2} \right) \int_{10^{-8}}^{10^{-6}} \text{STRINT}(\lambda) d\lambda = 8.26617 \Omega \cdot 10^{-9} \quad (6.4)$$

In 6.4, $\text{STRINT}(\lambda)$ [$\frac{\text{W}}{\text{m}^2 \cdot \text{nm}}$] is the representative spectrum of a 0th magnitude star, $\text{QE}(\lambda)$ is the quantum efficiency spectrum of the observing sensor, $\text{ATM}(\lambda)$ is the atmospheric transmission spectrum, λ [m] is wavelength, h [$\frac{\text{m}^2 \cdot \text{kg}}{\text{s}}$] is Plank's constant, and c [$\frac{\text{m}}{\text{s}^2}$] is the speed of light in vacuum.

6.1.4 Magnitudes per Square Arcsecond

A second surface brightness unit is $\left[\frac{\text{mag}}{\text{arcsec}^2} \right]$, also known as MPSAS (magnitudes per square arcsecond) or SQM (sky quality meter). This quantity can be thought of as a generalized S_{10} , where instead of quantifying the number of stars of a certain magnitude in a solid

angle, we measure the equivalent magnitude of a single point source. A surface brightness B_{10} in S_{10} can be converted into surface brightness B_{mag} in $\left[\frac{mag}{arcsec^2}\right]$ via Eq 6.5.

$$B_{mag} = -2.5 \log_{10} \left(\frac{B_{10} \cdot 10^{-4}}{12960000} \right) \quad (6.5)$$

In Eq 6.5 we first convert S_{10} to the total irradiance per square degree, convert square degrees to square arcseconds, and transform the result back into apparent magnitude. We can convert from MPSAS to irradiance per steradian via Eq 6.6 using 6.2.

$$I = \left(\frac{180}{3600\pi} \right)^2 I_0 \cdot 10^{-\frac{MPSAS}{2.5}} \quad (6.6)$$

6.1.5 Candela

Some light pollution datasets are given in units that include candela. Candela is the SI base unit of luminous intensity defined by the International Committee for Weights and Measures as "Fixing the numerical value of the luminous efficacy of monochromatic radiation of frequency $540 \cdot 10^{12}$ Hz to be equal to exactly 683" [35]. This means that an isotropic source with frequency $540 \cdot 10^{12}$ Hz ($\lambda = 555$ nm) has a luminous efficacy of $K_{cd} = 683$ [lm/W] where lm stands for lumens. Luminous efficacy itself determines how well a source produces visible light. For a given wavelength, we convert from candela B_{cd} to watts per steradian B_{wsr} via 6.7.

$$B_{wsr}(\lambda) = \frac{B_{cd}}{K_{cd}(\lambda)} \quad (6.7)$$

The luminous efficiency function $K_{cd}(\lambda)$ models the human eye's response to the visible spectrum [36]. Different fits of this function exist; we adopt that of Sharpe et al. [36], displayed in Figure 6.1.

Candela per unit area can be converted into MPSAS by combining Eq 6.7 with 6.1, yielding Eq 6.8, which is still a function of the source's wavelength.

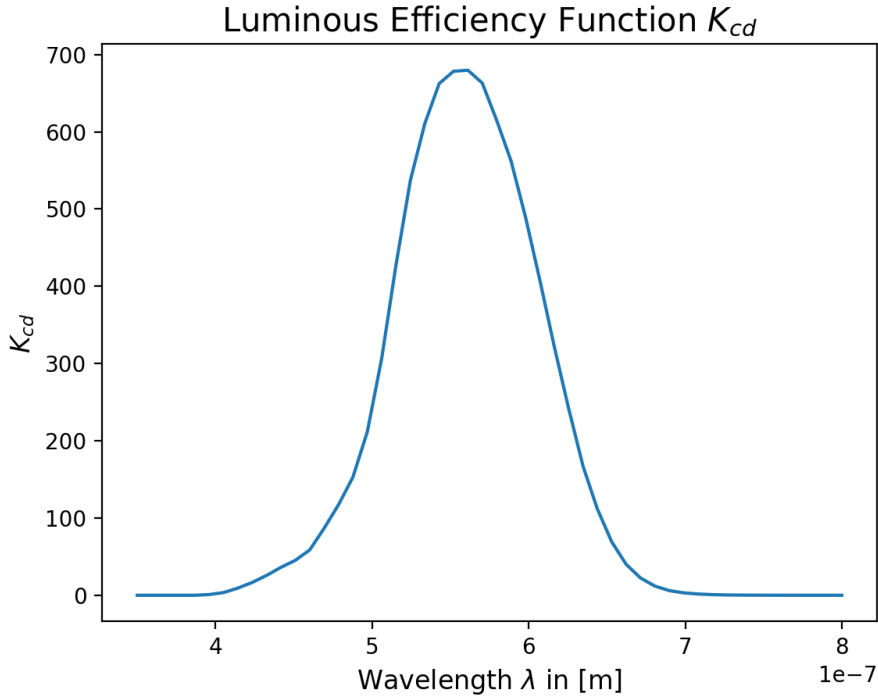


Figure 6.1. Luminous efficiency function from [36]

$$MPSAS(\lambda) = -2.5 \log_{10} \left(\frac{B_{cd}}{\left(\frac{180}{3600\pi} \right)^2 K_{cd}(\lambda) I_0} \right) \quad (6.8)$$

6.1.6 Photoelectron Counts

Raw observations of brightness taken by a CCD-equipped telescope are measured in photoelectron counts, otherwise known as Analog-to-Digital Units (ADU) [37]. The count in a single pixel obtained is directly proportional (via the ADU gain) to the number of photons incident on that pixel during the integration time. Higher order effects in the silicon of the CCD makes this statement incomplete at best, but for the non-resolved imaging applications we're concerned about, chip-level innacuracies besides readout noise and dark current are often neglected [38]. Irradiance can be converted back and forth to ADU via the conversion factor $SINT$ in Eq 6.9 [37].

$$\text{SINT} = \frac{\pi D^2}{4} \int_{10^{-8}}^{10^{-6}} \left(\frac{\text{SUN}(\lambda)}{I_{\text{sun}}} \right) \cdot \text{QE}(\lambda) \cdot \text{ATM}(\lambda) \cdot \left(\frac{\lambda}{hc} \right) d\lambda \quad (6.9)$$

In Eq 6.9, $\text{SUN}(\lambda)$ is the spectrum of solar irradiance in $\left[\frac{W}{m^2 \cdot m} \right]$, I_{sun} is the irradiance of the Sun (generally taken to be the solar constant 1361 $\left[\frac{W}{m^2} \right]$). Read literally, the integral term as units $\left[\frac{1}{Ws} \right]$, giving the number of counts per incident Watt of solar radiation and second of integration time. The aperture diameter factor outside the integral accounts for the area of light incident on the CCD, giving SINT units of $\left[\frac{m^2}{Ws} \right]$. Multiplying by irradiance in $\left[\frac{W}{m^2} \right]$ and an integration time Δt in seconds will yield the count of photoelectrons S in ADU as shown in Eq 6.10.

$$S = \text{SINT} \cdot I \cdot \Delta t \quad (6.10)$$

For completeness, irradiance can be recovered from a signal in ADU and the integration time via Eq 6.11.

$$I = \frac{S}{\text{SINT} \cdot \Delta t} \quad (6.11)$$

6.2 Astronomical Spectra

Four of the quantities needed for the background model vary with wavelength. These are the atmospheric transmission, the sensor quantum efficiency, the irradiance of a 0th magnitude star, and the solar spectrum. Atmospheric transmission is a unitless quantity conveying the fraction of light that is not absorbed by the atmosphere. Quantum efficiency is a unitless quantity which conveys the fraction of incident photons which are (proportionally) converted to photoelectrons in the CCD sensor. Each spectrum is displayed in Figure 6.2.

In practice, the quantum efficiency curve varies by sensor and the thermal conditions of the observation. The curve adopted in this work is that used by Krag; modern sensors will often perform better.

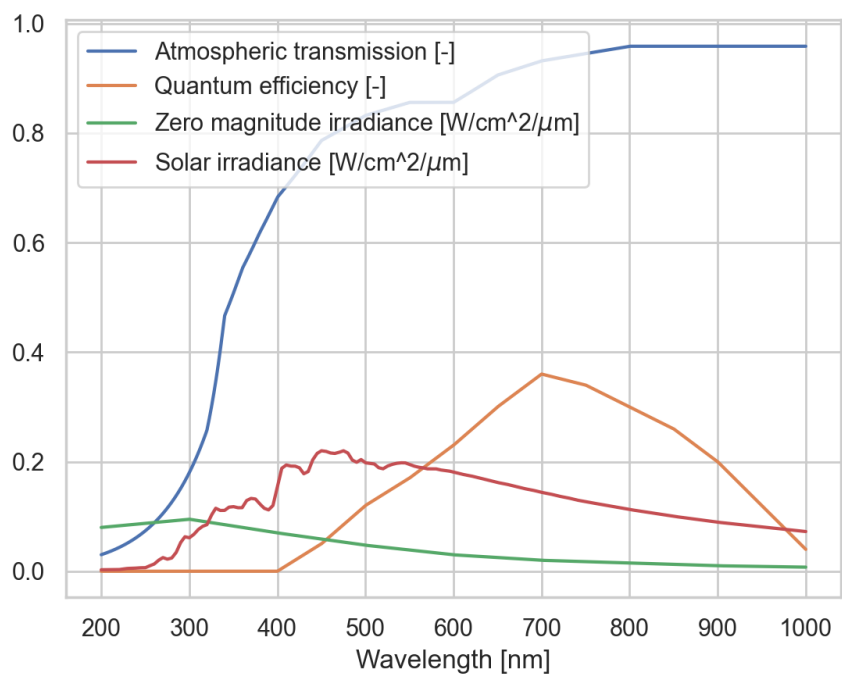


Figure 6.2. Astronomical Spectra

7. Background Signals

Whenever an optical telescope is observing a space object, the object's signal is necessarily superimposed on whatever signals exist in the background. In this context, background does not only refer to sources physically further than the object, but all sources that impact the image apart from the object signal. As we will see, some of these sources even originate within the telescope. To faithfully simulate a telescope observing an object, many position-based SDA tasks are able to ignore background effects while acquiring or tracking objects. For photometry-based SDA, the background is critical. Background signals can be broken up into atmospheric effects, exoatmospheric effects, and sensor effects.

7.1 Atmospheric Effects

7.1.1 Airglow

Certain chemical reactions from 80-110 km altitude in the upper atmosphere release visible light [37]. This effect is known as airglow. Since these reactions are assumed to be isotropic — equally intense when integrated along any vertical line extending upwards from the surface. We model the airglow signal AINT in a similar fashion to integrated starlight. Given the airglow spectra GLINT(λ) $\left[\frac{W}{m^2 \cdot m \cdot rad^2}\right]$, we compute Eq 7.1.

$$AINT = \frac{\pi D^2}{4} \int_{10^{-8}}^{10^{-6}} GLINT(\lambda) \cdot QE(\lambda) \cdot ATM(\lambda) \cdot \left(\frac{\lambda}{hc}\right) d\lambda \quad (7.1)$$

The quantity AINT has units $\left[\frac{1}{s \cdot rad^2}\right]$, meaning that the mean airglow signal in ADU per pixel is simply given by Eq 7.2

$$\bar{S}_{airglow} = AINT \cdot \frac{1}{\cos(\theta_z)} \cdot \Delta t \cdot \left(\frac{\pi s_{pix}}{648000}\right)^2 \quad (7.2)$$

In Eq 7.2, $\frac{1}{\cos(\theta_z)}$ is known as the Van Rhijn factor, which accounts for the accumulation of airmass near the horizon ??.

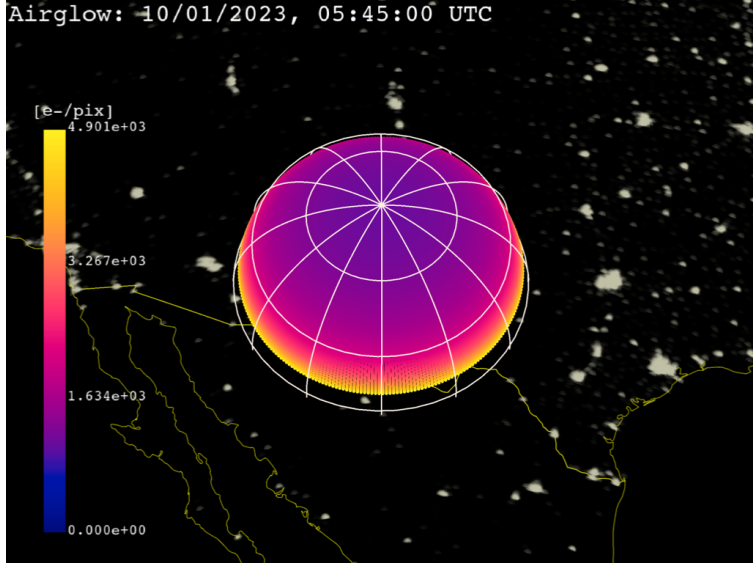


Figure 7.1. Mean airglow signal on the local observer hemisphere. The observer is in New Mexico, USA at 32.900° N, -105.533° W

7.1.2 Light Pollution

The final source of background noise light pollution. On a cloudless night with negligible light pollution, the zenith surface brightness is approximately $22 \left[\frac{mag}{arcsec^2} \right]$ (MPSAS) [37]. As light pollution increases, this zenith brightness may dip down to $14 - 15 \left[\frac{mag}{arcsec^2} \right]$. To get accurate localized zenith brightness values, we use the 2015 World Atlas of Sky Brightness dataset [39]. The data is reported in $\left[\frac{mcd}{cm^2} \right]$ on a 30-arcsecond grid, requiring us to convert to MPSAS. A subset of the global dataset is displayed in 7.2 This conversion is listed in Eq 6.8, using a monochromatic $\lambda = 474$ nm to fit Falchi et al.'s example conversions [40].

The mean light pollution CCD signal in ADU per pixel is formulated similarly to airglow. Given the station's zenith surface brightness $B_{poll,z}$ in MPSAS, we first convert to irradiance per steradian via 6.6, which we then input into 7.3 to compute the mean signal in ADU per pixel. Note that Krag does not implement a specific light pollution model, but instead takes the dark sky site zenith brightness of 22 MPSAS as an input to an atmospherically scattered light model. Here we simply use that model's formulation with a variable zenith brightness.

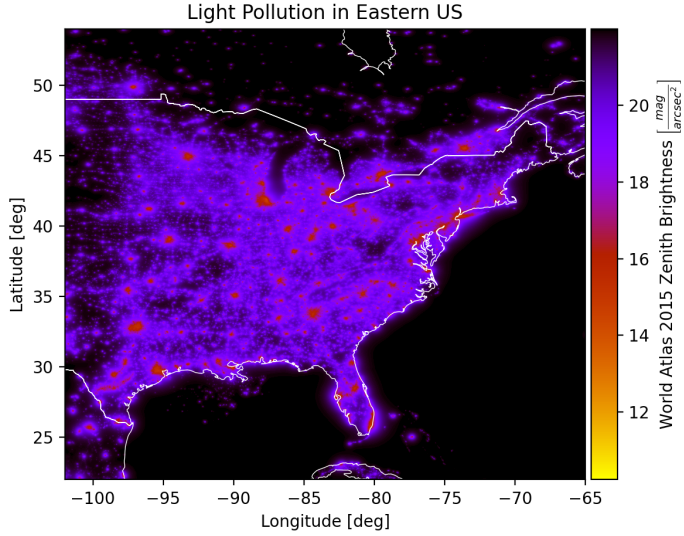


Figure 7.2. Zenith light pollution in the eastern USA, data from [39]

$$\bar{S}_{pollution} = B_{poll,z} \cdot SINT \cdot \frac{1}{\cos(\theta_z)} \cdot \Delta t \cdot \left(\frac{\pi s_{pix}}{648000} \right)^2 \quad (7.3)$$

7.1.3 Twilight

Even after the Sun sets, scattered sunlight in the upper atmosphere creates a signal on our CCD. The twilight model implemented for this work is due to Patat et al. and was developed for the European Southern Observatory at Paranal in Chile [41]. This model implements the zenith brightness as a function of the solar zenith angle γ — the angle from zenith to the Sun’s apparent centroid. Patat et al.’s model fits a second-degree polynomial in γ to approximately 2000 observations, yielding separate curves for each of the UBVRI passbands. For example, for the V band, the twilight zenith brightness in MPSAS is given by 7.4 [41].

$$B_{twi,z} = 11.84 + 1.518(\gamma - 95^\circ) - 0.057(\gamma - 95^\circ)^2 \quad (7.4)$$

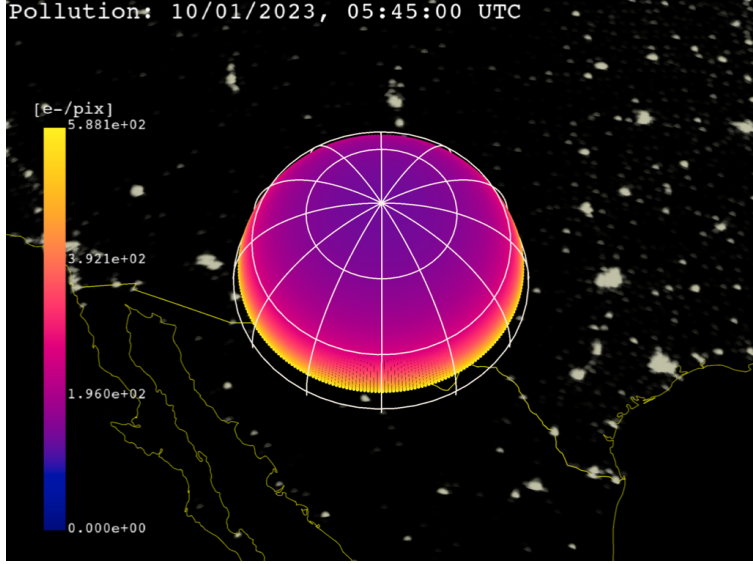


Figure 7.3. Mean light pollution signal on the local observer hemisphere. The observer is in New Mexico, USA at 32.900° N, -105.533° W

Eq 7.4 is valid from $95^{\circ} \leq \gamma \leq 105^{\circ}$. Before $\gamma 95^{\circ}$, we take the zenith brightness to be constant and equal to the brightness at $\gamma 95^{\circ}$. This is not accurate, but is sufficiently bright to correctly forbid daytime observations by lowering the SNR drastically. After $\gamma = 105^{\circ}$ we set the zenith surface brightness to $B_{twi,z} == 22$ MPSAS to match the optimal observation condition of the light pollution model [37]. Zenith twilight brightness is plotted as a function of γ in Figure ??.

Computing the mean CCD signal in ADU per pixel due to the twilight brightness proceeds identically to the light pollution formulation.

$$\bar{S}_{twilight} = B_{twi,z} \cdot SINT \cdot \frac{1}{\cos(\theta_z)} \cdot \Delta t \cdot \left(\frac{\pi s_{pix}}{648000} \right)^2 \quad (7.5)$$

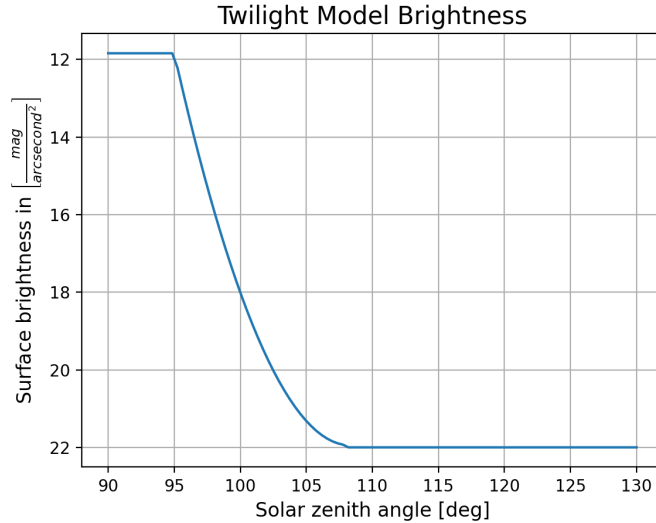


Figure 7.4. Twilight model surface brightness at zenith as a function of solar zenith angle

7.2 Exoatmospheric Effects

7.2.1 Integrated Starlight

Stars are almost always present in optical images of space objects. The brightest stars streaking across the field of view in Figure 7.5 have high SNRs and stand out clearly against the dark background. This raises a question: if we're observing a full $1^\circ \times 1^\circ$ area of the sky, where are the rest of the stars given that the Milky Way alone contains approximately $1 \cdot 10^{11}$ stars? The answer is relatively obvious: many more stars are present in the image than we can pick out individually, most of them fall into the background. We call this residual faint starlight "integrated" starlight as we are effectively integrating the signals from thousands or millions of stars across the image plane.

In Figure 7.6, most stars are too faint to appear as points of light on the image plane. Instead, they merge into the background. The signal due to these faint stars is known as integrated starlight. Krag [37] modeled this signal by building a $1^\circ \times 1^\circ$ grid of surface brightness values for the full right ascension (RA) and declination (Dec) sphere. Krag used the Guide Star catalog, which contains 15 million stars down to magnitude 16. Exponential

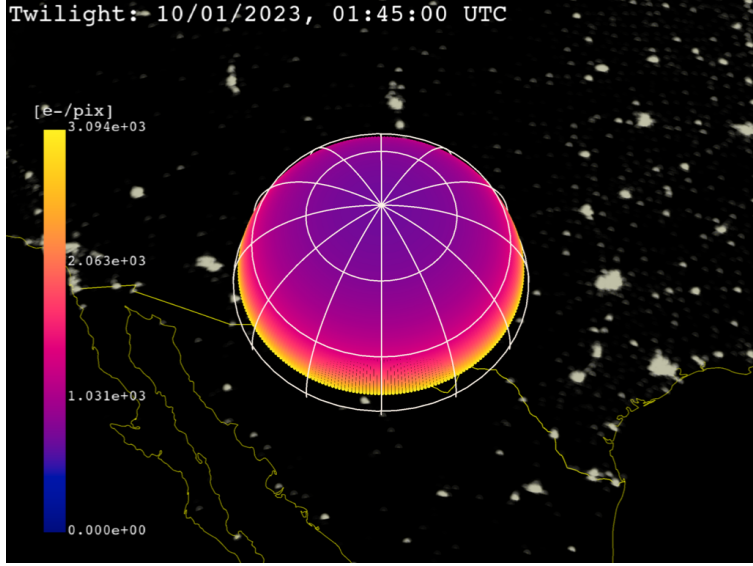


Figure 7.5. Mean twilight signal on the local observer hemisphere. The observer is in New Mexico, USA at $32.900^\circ \text{ N}, -105.533^\circ \text{ W}$

extrapolation was used to predict star counts in each bin for higher magnitudes [37]. Twenty years later, we have access to larger star catalogs that are nearly complete to much dimmer magnitudes. The integrated starlight catalog used in this work was built from the GAIA catalog with approximately 1.5 billion stars down to magnitude 21-22 [42]. The same $1^\circ \times 1^\circ$ grid was computed using the `astroquery.gaia` Python package [43]. Figure 7.7 shows the computed patched catalog, in units of S_{10} .

Now that we have a data source for the exoatmospheric mean brightness of the night sky due to integrated starlight, we can compute the corresponding signal mean for a telescope equipped with a CCD sensor. Again, we adopt Krag's formulation [37].

$$\text{BINT} = \frac{\pi D^2}{4} \int_{10^{-8}}^{10^{-6}} \text{STRINT}(\lambda) \cdot \text{QE}(\lambda) \cdot \text{ATM}(\lambda) \cdot \left(\frac{\lambda}{hc} \right) d\lambda \quad (7.6)$$

In Eq 7.6, D is the telescope aperture diameter in meters, h is Plank's constant in $\left[\frac{m^2 kg}{s} \right]$, and c is the speed of light in vacuum in $\left[\frac{m}{s} \right]$. The resulting quantity BINT has units of $\left[\frac{1}{s} \right]$, representing the mean total photons passing through the telescope aperture due to integrated starlight.



Figure 7.6. Raw image of three GEO objects with stars streaking through the background. Taken by the Purdue Optical Ground station at 32.900° N, -105.533° W by Nathan Houtz

$$\bar{S}_{star} = 10^{-4} \cdot BINT \cdot \left(\frac{s_{pix}}{3600} \right)^2 \cdot \Delta t \cdot b_{cat} \quad (7.7)$$

In Eq 7.7, b_{cat} is the patched catalog brightness in $[S_{10}]$, s_{pix} is the telescope pixel scale in $\left[\frac{\text{arcsecond}}{\text{pix}} \right]$, and Δt is the integration time in seconds. Note the addition of the 10^{-4} factor to reconcile catalog surface brightness in terms of 10th magnitude stars, and the 0th magnitude source in BINT. This yields \bar{S}_{star} with units $\left[\frac{\text{e}^-}{\text{pix}^2} \right]$; photoelectron counts (ADU) per pixel. Figure 7.8 shows the background signal mean due to integrated starlight.

7.2.2 Scattered Moonlight

Moonlight scattering through the atmosphere significant increases background brightness [37]. This scattering effect can be decomposed into Rayleigh (isotropically distributed) and Mie (exponentially distributed) scattering modes. The Rayleigh scattered component is computed with Table 4 published by Daniels parameterized by the angle from the observation

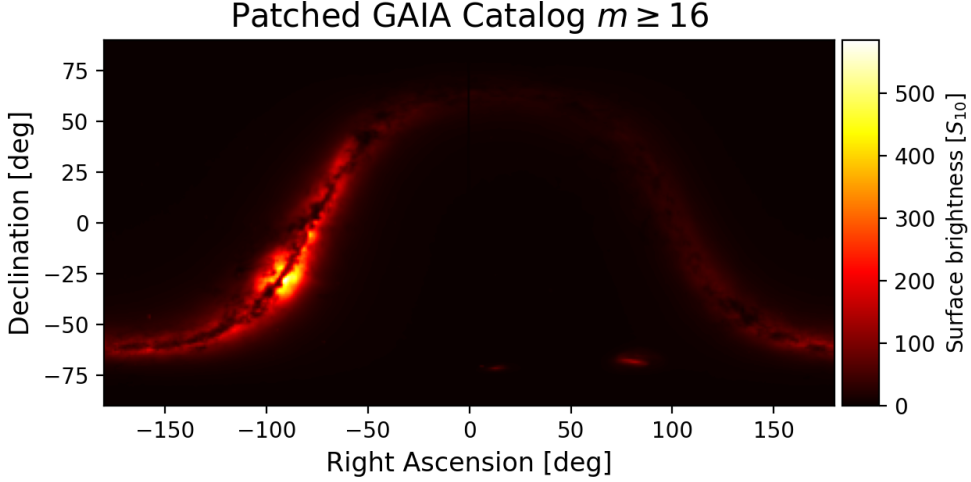


Figure 7.7. Integrated starlight patched catalog

to zenith z_{obs} , the angle from the Moon to zenith z_{moon} , and the angle between the observation and the Moon on the horizon ΔAz [44]. Interpolating this table yields the intensity of the Rayleigh scattering F_{rs} in $10^{-10} W/(cm^2 \cdot \mu m \cdot sr)$ [37]. The Mie scattered component is formulated with Eq 7.8.

$$F_{ms}(\lambda) = a_1 \left[e^{-\left(\frac{\Psi}{\Psi_1}\right)} + a_2 e^{-\left(\frac{\pi-\Psi}{\Psi_2}\right)} \right] F_{rs}(\lambda) \quad (7.8)$$

Daniels recommends $a_1 \in [50, 100]$, $a_2 \in [0.01, 0.02]$, $\Psi_1 \in [10^\circ, 20^\circ]$, and $\Psi_2 \approx 50$ [44]. Prior to any station-specific fitting, we choose the middle of these intervals, yielding $a_1 = 75$, $a_2 = 0.015$, $\Psi_1 = 15^\circ$, and $\Psi_2 = 50^\circ$. a_1 and a_2 are dimensionless, such that F_{ms} also has units of $10^{-10} W/(cm^2 \cdot \mu m \cdot sr)$, allowing us to compute the total intensity of the scattered moonlight F_{mt} via Eq 7.9 following Krag's formulation [37].

$$F_{mt} = f(\theta) [F_{rs}(\lambda) + F_{ms}(\lambda)] \quad (7.9)$$

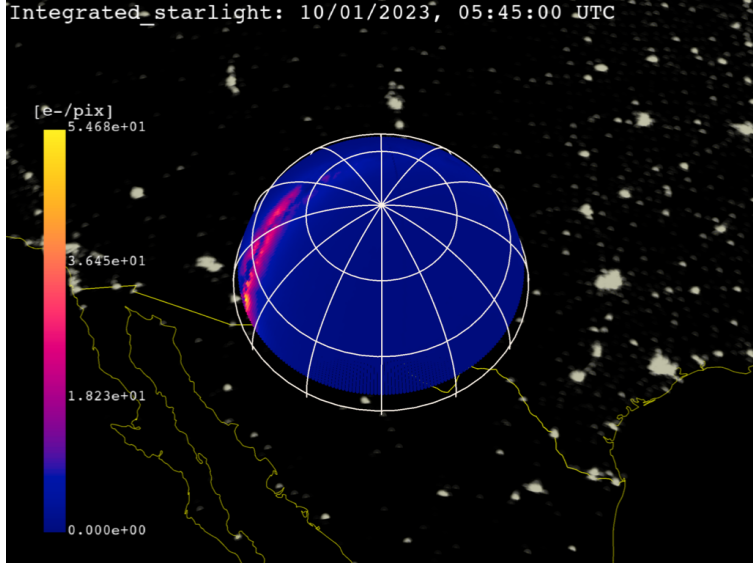


Figure 7.8. Integrated starlight signal on the local observer hemisphere. The observer is in New Mexico, USA at 32.900° N, -105.533° W

in Eq 7.9, $f(\theta)$ is the lunar phase function which describes the fraction of the full Moon brightness is reflected at an observer viewing the Moon an angle θ from the Sun vector. This function is linearly interpolated within Table 3 in [44]. Finally, Krag introduces a correction factor f_{corr} to account for the difference between the Sun’s irradiance spectrum and the spectrum of scattered moonlight, defined in Eq 7.10.

$$f_{corr} = \frac{I_0}{SUN(550 \text{ [nm]})} \quad (7.10)$$

With all these pieces, we can put together the mean scattered moonlight signal in ADU per pixel in Eq 7.11.

$$\bar{S}_{moon} = F_{mt}(550 \text{ [nm]}) \cdot SINT \cdot \left(\frac{s_{pix}}{3600} \right)^2 \cdot \Delta t \cdot f_{corr} \quad (7.11)$$

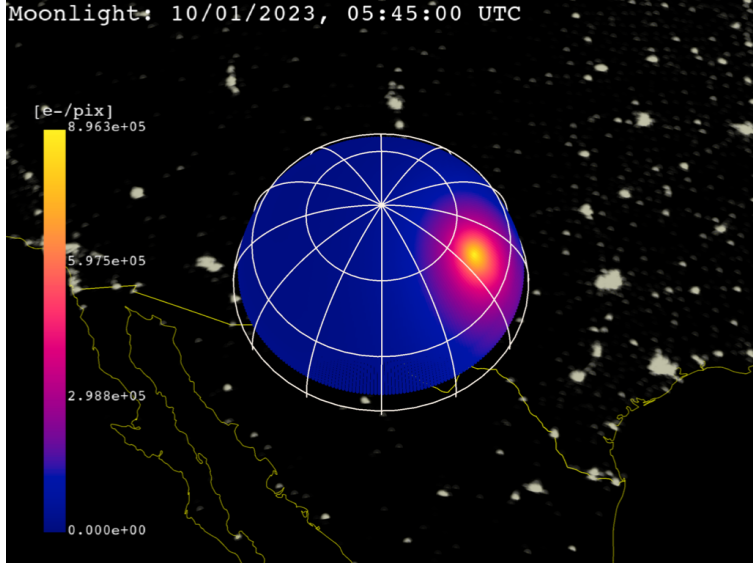


Figure 7.9. Mean scattered moonlight signal on the local observer hemisphere. The observer is in New Mexico, USA at 32.900° N, -105.533° W

7.2.3 Zodiacal Light

Zodiacal light is an effect created by sunlight reflecting off of dust in the ecliptic plane [37]. Zodiacal light is strongest around the Sun — an area that is not of interest for us — but also reaches a peak directly away from the Sun due to the opposition effect. This peak is known as the Gegenschein, meaning "opposing light". We compute the of the zodiacal light via Table 1 of [45]. This reports the surface brightness of the zodiacal light in S_{10} , which we use without conversion to find the mean CCD signal in ADU per pixel via Eq 7.12.

$$\bar{S}_{zod} = BINT \cdot \left(\frac{s_{pix}}{3600} \right)^2 \cdot \Delta t \cdot ZOD \cdot 10^{-4} \quad (7.12)$$

As in the integrated starlight signal, the 10^{-4} factor reconciles the S_{10} surface brightness with the 0th magnitude source in BINT.

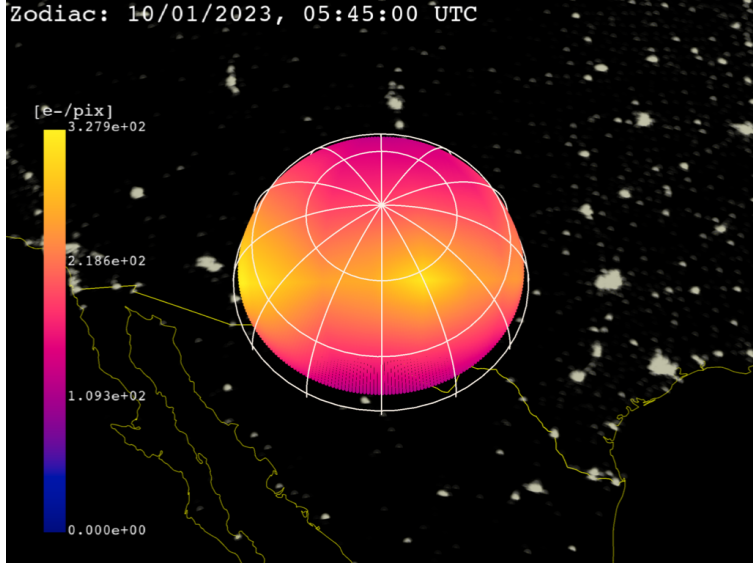


Figure 7.10. Mean zodiacal light signal on the local observer hemisphere. The observer is in New Mexico, USA at 32.900° N, -105.533° W

7.2.4 Sampling Background

Notice that each background signal is only defined in terms of its mean. On a pixel-by-pixel basis, the signal for an exposure is sampled from a Poisson distribution for each background term. This distribution can be interpreted as modeling the number of independent events that occur during a time period. In our case, this translates to individual photons being incident on our sensor. A Poisson distribution is defined on the positive integers by a single parameter λ which is both the mean and variance of the distribution. The probability density function (PDF) for the Poisson distribution takes the form of Eq 7.13 [38].

$$P_{\lambda}(x = k) = \frac{\lambda^k e^{-\lambda}}{k!} \quad (7.13)$$

This distribution has a useful property that $P_{\lambda_1+\lambda_2}(x = k) = P_{\lambda_1}(x = k) + P_{\lambda_2}(x = k)$ so long as the distributions described by λ_1 and λ_2 are independent. Since our background sources are assumed to be independent as sources like moonlight and zodiacal light are clearly distinct; if the Moon vanished, interplanetary dust across the solar system would reflect light

Signal source	Magnitude [e ⁻ /pix]
Airglow	$10^3 - 10^4$
Scattered moonlight	$0 - 10^5$
Integrated starlight	$10^1 - 10^2$
Light pollution	$10^2 - 10^3$
Zodiacal light	$10^2 - 10^4$
Twilight	$10^1 - 10^7$

Table 7.1. Background signal importance

identically. This means that we can formulate the total background signal as a single Poisson variable.

$$\lambda_{background} = \bar{S}_{airglow} + \bar{S}_{pollution} + \bar{S}_{twilight} + \bar{S}_{star} + \bar{S}_{moon} + \bar{S}_{zod} \quad (7.14)$$

To compute the background of the CCD image, we simply sample from the Poisson distribution defined by $\lambda_{background}$.

7.2.5 Background Source Importance

Some background signals are more impactful than others. Table ?? details the approximate magnitudes in photoelectrons per pixel one can expect from a telescope similar to the Purdue Optical Ground Station.

7.3 Sensor Effects

7.3.1 Dark Noise

7.3.2 Readout Noise

8. Light Curve Simulation

8.0.1 Simulating Convex Objects

Light curve simulation for convex geometry can be solved semi-analytically as each facet's contribution to the measured irradiance can be computed individually [1]. Determining whether a face is illuminated requires two horizon checks to determine visibility from the Sun and to the observer. For a facet i at timestep j these horizon checks are expressed by the shadowing condition μ_{ij} .

$$\mu_{ij} = \begin{cases} 1 & \text{if } (\hat{O}_j \cdot \hat{n}_i) > 0 \text{ and } (\hat{S}_j \cdot \hat{n}_i) > 0 \text{ and } \delta_{ij,ss} = 0 \text{ and } \delta_{ij,os} = 0 \\ 0 & \text{otherwise} \end{cases} \quad (8.1)$$

The unit vectors \hat{O} and \hat{S} point from the center of mass of the object to the observer and Sun, respectively. We choose the outward-pointing facet normal unit vector \hat{n} by convention for all mesh operations. The self-shadowing and observer-shadowing conditions, $\delta_{ij,ss}$ and $\delta_{ij,os}$, are always zero for convex polyhedra but are crucial for accurately simulating non-convex geometry. For objects with concavities, self-shadowing refers to shadows cast by an object onto itself and observer-shadowing refers to otherwise visible faces blocked by other portions of the geometry.

The irradiance I received by the observer at timestep j is the sum of the received irradiance from all facets, composed of specular and diffuse contributions. We express each contribution as the product of the normalized irradiance \hat{I} . This can be scaled to adjust for the distance from the observer to the object to yield the noiseless received irradiance.

9. Appendices

9.1 Astronomical Spectra Data

Atmospheric Extinction

```
{"lambda": [0.0, 3.2e-07, 3.400000000000003e-07, 3.6e-07, 3.79999999999996e-07,  
4e-07, 4.5e-07, 5e-07, 5.5e-07, 6e-07, 6.5e-07, 7e-07, 8e-07, 0.001], "extinction":  
[5.0, 0.96, 0.54, 0.42, 0.34, 0.27, 0.17, 0.13, 0.11, 0.11, 0.07, 0.05, 0.03, 0.0]}}
```

Quantum Efficiency

```
{"lambda": [4.000000000000003e-07, 4.500000000000003e-07, 5.000000000000001e-07,  
5.5e-07, 6.000000000000001e-07, 6.5e-07, 7.000000000000001e-07, 7.5e-07,  
8.000000000000001e-07, 8.5e-07, 9.000000000000001e-07, 9.5e-07,  
1.000000000000002e-06, 1.050000000000001e-06], "quantum_efficiency": [0.0, 0.05,  
0.12, 0.17, 0.23, 0.3, 0.36, 0.34, 0.3, 0.26, 0.2, 0.12, 0.04, 0.0]}{}
```

9.1.1 Background Source Data

Lunar Phase Factor

```
{"phase_factor": [1.00, 0.809, 0.685, 0.483, 0.377, 0.288, 0.225, 0.172, 0.127, 0.089,  
0.061, 0.041, 0.077, 0.017, 0.009, 0.004, 0.001, 0.0, 0.0], "phase_angle": [0,  
0.17453293, 0.34906585, 0.52359878, 0.6981317 , 0.87266463, 1.04719755, 1.22173048,  
1.3962634 , 1.57079633, 1.74532925, 1.91986218, 2.0943951 , 2.26892803, 2.44346095,  
2.61799388, 2.7925268 , 2.96705973, 3.14159265]}{}
```

Scattered Moonlight

```
{"z_obs": [0.0, 0.17453292519943295, 0.3490658503988659, 0.5235987755982988,  
0.6981317007977318, 0.8726646259971648, 1.0471975511965976, 1.2217304763960306,  
1.3962634015954636], "delta_az": [0.0, 0.7853981633974483, 1.5707963267948966,  
2.356194490192345, 3.141592653589793], "z_moon": [0.0, 0.5235987755982988,  
1.0471975511965976, 1.3089969389957472], "radianc": [[[22.0, 19.0, 13.0, 10.0],  
[22.0, 19.0, 13.0, 10.0], [22.0, 19.0, 13.0, 10.0], [22.0, 19.0, 13.0, 10.0], [22.0,  
19.0, 13.0, 10.0]], [[22.0, 21.0, 15.0, 11.0], [22.0, 20.0, 14.0, 11.0], [22.0,  
19.0, 13.0, 10.0], [22.0, 18.0, 12.0, 9.7], [22.0, 18.0, 12.0, 9.6]], [[22.0, 23.0,  
18.0, 13.0], [22.0, 22.0, 16.0, 12.0], [22.0, 19.0, 14.0, 10.0], [22.0, 17.0, 12.0,  
9.9], [22.0, 17.0, 12.0, 10.0]], [[22.0, 25.0, 21.0, 16.0], [22.0, 23.0, 18.0,  
14.0], [22.0, 20.0, 14.0, 11.0], [22.0, 17.0, 12.0, 11.0], [22.0, 16.0, 12.0,  
11.0]], [[23.0, 28.0, 25.0, 20.0], [23.0, 25.0, 21.0, 17.0], [23.0, 21.0, 16.0,  
12.0], [23.0, 17.0, 14.0, 13.0], [23.0, 16.0, 14.0, 14.0]], [[24.0, 31.0, 31.0,  
25.0], [24.0, 28.0, 26.0, 20.0], [24.0, 22.0, 18.0, 15.0], [24.0, 18.0, 17.0, 16.0],  
[24.0, 18.0, 18.0]], [[27.0, 37.0, 39.0, 33.0], [27.0, 33.0, 32.0, 26.0],  
[27.0, 25.0, 22.0, 18.0], [27.0, 22.0, 22.0, 21.0], [27.0, 22.0, 25.0, 26.0]],  
[[34.0, 47.0, 54.0, 48.0], [34.0, 41.0, 43.0, 37.0], [34.0, 33.0, 29.0, 25.0],  
[34.0, 30.0, 33.0, 32.0], [34.0, 31.0, 40.0, 40.0]], [[55.0, 72.0, 89.0, 82.0],  
[55.0, 65.0, 71.0, 63.0], [55.0, 54.0, 50.0, 43.0], [55.0, 54.0, 61.0, 58.0], [58.0,  
58.0, 76.0, 75.0]]]}
```

Zodiacal Light

```
{"ecliptic_lat": [0.0, 0.17453292519943295, 0.3490658503988659, 0.5235987755982988, 0.6981317007977318, 0.8726646259971648, 1.0471975511965976, 1.2217304763960306, 1.3962634015954636], "ecliptic_lon": [3.141592653589793, 2.792526803190927, 2.443460952792061, 2.0943951023931953, 1.7453292519943295, 1.3962634015954636, 1.1344640137963142, 1.0471975511965976, 0.9599310885968813, 0.8726646259971648, 0.7853981633974483, 0.6981317007977318, 0.6108652381980153, 0.5235987755982988, 0.4363323129985824, 0.3490658503988659, 0.2617993877991494, 0.17453292519943295, 0.08726646259971647, 0.0], "brightness": [[[258.0, 211.0, 206.99999999999997, 239.0, 277.0, 365.0, 535.0, 630.0, 756.0, 939.0, 1190.0, 1490.0, 2010.0000000000002, 2940.0, 4660.0, 7690.000000000001, 15100.0, 36500.0, 176000.0, 163000000.0], [212.0, 194.0, 185.0, 217.0, 247.0000000000003, 312.0, 418.0, 455.0, 512.0, 603.0, 696.0, 825.0, 1150.0, 1550.0, 1820.0, 2140.0, 2760.0, 2720.0, 5630.0, 19900.0], [183.0, 174.0, 168.0, 196.0, 220.0000000000003, 258.0, 330.0, 339.0, 358.0, 403.0, 442.0, 512.0, 635.0, 800.0, 932.0, 1070.0, 1120.0, 1390.0, 1700.0, 2290.0], [159.0, 153.0, 152.0, 177.0, 196.0, 219.0, 258.0, 270.0, 282.0, 290.0, 304.0, 331.0, 363.0, 417.0, 491.0, 542.0, 592.0, 655.0, 724.0, 794.0], [141.0, 137.0, 137.0, 161.0, 175.0, 190.0, 204.0, 212.0, 229.0, 227.0, 233.0, 240.0, 224.0000000000003, 241.0, 246.0, 252.0, 265.0, 290.0, 315.0, 403.0], [127.0, 127.0, 128.0, 146.0, 156.0, 166.0, 165.0, 166.0, 183.0, 185.0, 189.0, 186.0, 171.0, 180.0, 183.0, 186.0, 190.0, 199.0, 209.0, 252.0], [117.0, 120.0, 120.0, 132.0, 139.0, 146.0, 137.0, 137.0, 147.0, 149.0, 150.0, 149.0, 137.0, 141.0, 144.0, 145.0, 145.0, 145.0, 146.0, 150.0], [110.0000000000001, 112.0000000000001, 112.0000000000001, 120.0, 123.0, 127.0, 118.0, 120.0, 124.0, 124.0, 124.0, 126.0, 118.0, 120.0, 121.0, 121.0, 121.0, 121.0, 121.0], [103.0, 105.0, 105.0, 108.0, 111.0000000000001, 111.0000000000001, 106.0, 107.0, 107.0, 108.0, 107.0, 111.0000000000001, 107.0, 106.0, 108.0, 108.0, 108.0, 108.0, 108.0]]}
```

9.1.2 Telescope Parameters

Purdue Optical Ground Station

Parameter	Value
FWHM	1.5
Sensor dimensions	$0.03690 \times 0.03690 [m]$
<i>f</i> number	7.2
Aperture diameter	0.35560 [m]
Secondary diameter	0.1724660 [m]
Sensor pixels	4096×4096
Pixel size	$9.009 \cdot 10^{-6} [m/\text{pix}]$
Pixel scale	0.72545 [<i>arcsec</i>]
Field of view	$0.824425^\circ \times 0.824425^\circ$
Integration time	1 [s]

Table 9.1. Purdue Optical Ground Station telescope parameters

REFERENCES

- [1] M. Kaasalainen, J. Torppa, and K. Muinonen, “Optimization methods for asteroid lightcurve inversion: II. the complete inverse problem,” *Icarus*, vol. 153, no. 1, pp. 37–51, 2001, ISSN: 0019-1035. DOI: <https://doi.org/10.1006/icar.2001.6674>. [Online]. Available: <https://www.sciencedirect.com/science/article/pii/S0019103501966746>.
- [2] S. Fan, C. Frueh, and A. Buzzoni, “A light curve simulation of the apollo lunar ascent module,” in *AIAA/AAS Astrodynamics Specialist Conference*, 2016, pp. 1–10. DOI: [10.2514/6.2016-5504](https://doi.org/10.2514/6.2016-5504).
- [3] S. Fan, “The light curve simulation and its inversion problem for human-made space objects,” Ph.D. dissertation, Purdue University, Aug. 2020. DOI: [10.25394/PGS.12749570.v1](https://doi.org/10.25394/PGS.12749570.v1).
- [4] A. M. Friedman, “Observability analysis for space situational awareness,” Ph.D. dissertation, Purdue University, Apr. 2020. DOI: [10.25394/PGS.12196863.v1](https://doi.org/10.25394/PGS.12196863.v1).
- [5] D. Kobayashi and C. Frueh, “Compressed sensing for satellite characterization,” in *Proceedings of the 20th AAS/AIAA Astrodynamics Specialist Conference*, Aug. 2020, pp. 1–20.
- [6] C. Früh and M. K. Jah, “Coupled orbit attitude motion of high area-to-mass ratio (hamr) objects including efficient self-shadowing,” *Acta Astronautica*, vol. 95, pp. 227–241, 2014, ISSN: 0094-5765. DOI: <https://doi.org/10.1016/j.actaastro.2013.11.017>.
- [7] J. Allworth, L. Windrim, J. Wardman, D. Kucharski, J. Bennett, and M. Bryson, “Development of a high fidelity simulator for generalised photometric based space object classification using machine learning,” in *Proceedings of 70th International Astronautical Congress*, International Astronautical Congress, 2019, pp. 1–14. DOI: [10.48550/ARXIV.2004.12270](https://doi.org/10.48550/ARXIV.2004.12270). [Online]. Available: <https://arxiv.org/abs/2004.12270>.
- [8] J. Allworth, L. Windrim, J. Bennett, and M. Bryson, “A transfer learning approach to space debris classification using observational light curve data,” *Acta Astronautica*, vol. 181, pp. 301–315, Jan. 2021. DOI: [10.1016/j.actaastro.2021.01.048](https://doi.org/10.1016/j.actaastro.2021.01.048).
- [9] R. Furfaro, R. Linares, and V. Reddy, “Shape Identification of Space Objects via Light Curve Inversion Using Deep Learning Models,” in *Proceedings of the 20th Advanced Maui Optical and Space Surveillance Technologies Conference*, S. Ryan, Ed., Sep. 2019, 17, p. 17.

- [10] D. V. Cabrera, J. Utzmann, and R. Förstner, “Inversion of the shape of space debris from non-resolved optical measurements within spook,” in *Proceedings of the 22nd Advanced Maui Optical and Space Surveillance Technologies Conference*, 2021, pp. 1–18.
- [11] B. K. Bradley and P. Axelrad, “Lightcurve inversion for shape estimation of geo objects from space-based sensors,” in *Proceedings of the International Symposium on Space Flight Dynamics*, 2014, pp. 1–20.
- [12] R. Linares and J. L. Crassidis, “Space-object shape inversion via adaptive hamiltonian markov chain monte carlo,” *Journal of Guidance, Control, and Dynamics*, vol. 41, no. 1, pp. 47–58, 2018.
- [13] K. McNally, D. Ramirez, A. M. Anton, D. Smith, and J. Dick, “Artificial intelligence for space resident objects characterisation with lightcurves,” in *Proceedings of the 8th European Conference on Space Debris*, ESA Space Debris Office, 2021, pp. 1–12.
- [14] L. D. J. Blacketer, “Attitude characterisation of space objects using optical light curves,” Ph.D. dissertation, University of Southampton, Mar. 2022. [Online]. Available: <https://eprints.soton.ac.uk/457200/>.
- [15] C.-K. Chng, M. Sasdelli, and T.-J. Chin, “Globally optimal shape and spin pole determination with light-curve inversion,” *Monthly Notices of the Royal Astronomical Society*, vol. 513, no. 1, pp. 311–332, Jan. 2022, ISSN: 0035-8711. DOI: [10.1093/mnras/stac198](https://doi.org/10.1093/mnras/stac198). eprint: <https://academic.oup.com/mnras/article-pdf/513/1/311/43446894/stac198.pdf>. [Online]. Available: <https://doi.org/10.1093/mnras/stac198>.
- [16] B. Calef, J. Africano, B. Birge, D. Hall, and P. Kervin, “Photometric signature inversion,” in *Unconventional Imaging II*, V. L. Gamiz, P. S. Idell, and M. S. Strojnik, Eds., International Society for Optics and Photonics, vol. 6307, SPIE, 2006, pp. 141–150. DOI: [10.1117/12.683015](https://doi.org/10.1117/12.683015). [Online]. Available: <https://doi.org/10.1117/12.683015>.
- [17] S. Fan and C. Frueh, “A direct light curve inversion scheme in the presence of measurement noise,” *The Journal of the Astronautical Sciences*, vol. 67, Aug. 2019. DOI: [10.1007/s40295-019-00190-3](https://doi.org/10.1007/s40295-019-00190-3).
- [18] S. Fan and C. Frueh, “Multi-hypothesis light curve inversion scheme for convex objects with minimal observations,” in *Proceedings of the 8th European Conference on Space Debris*, ESA Space Debris Office, 2021, pp. 1–7.

- [19] A. M. Friedman and C. Frueh, “Observability of light curve inversion for shape and feature determination exemplified by a case analysis,” *Journal of the Astronautical Sciences*, vol. 69, no. 2, pp. 537–569, Apr. 2022. DOI: [10.1007/s40295-021-00293-w](https://doi.org/10.1007/s40295-021-00293-w).
- [20] R. Linares, M. Jah, and J. Crassidis, “Inactive space object shape estimation via astrometric and photometric data fusion,” *Advances in the Astronautical Sciences*, vol. 143, pp. 217–232, Jan. 2012.
- [21] R. Linares, M. K. Jah, J. L. Crassidis, and C. K. Nebelecky, “Space object shape characterization and tracking using light curve and angles data,” *Journal of Guidance, Control, and Dynamics*, vol. 37, no. 1, pp. 13–25, 2014. DOI: [10.2514/1.62986](https://doi.org/10.2514/1.62986).
- [22] R. Linares and R. Furfaro, “Space object classification using deep convolutional neural networks,” in *19th International Conference on Information Fusion*, Jul. 2016, pp. 1–8.
- [23] E. Kerr, G. P. Elisabeth, P. Talon, and D. Petit, “Using ai to analyse light curves for geo object characterisation,” in *Proceedings of the 22nd Advanced Maui Optical and Space Surveillance Technologies Conference*, 2021, pp. 1–9.
- [24] D. Hall, B. Calef, K. Knox, M. Bolden, and P. Kervin, “Separating attitude and shape effects for non-resolved objects,” in *The 2007 AMOS Technical Conference Proceedings*, Maui Economic Development Board, Inc. Kihei, Maui, HI, 2007, pp. 464–475.
- [25] D. O. Fulcoly, K. I. Kalamaroff, and F. K. Chun, “Determining basic satellite shape from photometric light curves,” *Journal of Spacecraft and Rockets*, vol. 49, pp. 76–82, 2012.
- [26] T. Yanagisawa and H. Kurosaki, “Shape and motion estimate of leo debris using light curves,” *Advances in Space Research*, vol. 50, no. 1, pp. 136–145, 2012, ISSN: 0273-1177. DOI: <https://doi.org/10.1016/j.asr.2012.03.021>.
- [27] D. Kobayashi and C. Frueh, “Compressed sensing for satellite characterization: Shadowing as a sensing matrix,” *8th European Conference on Space Debris*, vol. 8, Apr. 2021. DOI: [10.13140/RG.2.2.30685.33765](https://doi.org/10.13140/RG.2.2.30685.33765).
- [28] J. urech and M. Kaasalainen, “Photometric signatures of highly nonconvex and binary asteroids,” *Astronomy & Astrophysics*, vol. 404, no. 2, pp. 709–714, Jun. 2003. DOI: [10.1051/0004-6361:20030505](https://doi.org/10.1051/0004-6361:20030505).

- [29] M. Viikinkoski, J. Hanu, M. Kaasalainen, F. Marchis, and J. urech, “Adaptive optics and lightcurve data of asteroids: twenty shape models and information content analysis,” *Astronomy and Astrophysics*, vol. 607, pp. 1–14, Nov. 2017. DOI: [10.1051/0004-6361/201731456](https://doi.org/10.1051/0004-6361/201731456).
- [30] K. Ikeuchi, “Recognition of 3-d objects using the extended gaussian image.,” in *IJCAI*, 1981, pp. 595–600.
- [31] J. J. Little, “Extended gaussian images, mixed volumes, shape reconstruction,” in *Proceedings of the First Annual Symposium on Computational Geometry*, ser. SCG ’85, Baltimore, Maryland, USA: Association for Computing Machinery, 1985, pp. 15–23, ISBN: 0897911636. DOI: [10.1145/323233.323236](https://doi.org/10.1145/323233.323236). [Online]. Available: <https://doi.org/10.1145/323233.323236>.
- [32] B. Nicolet, A. Jacobson, and W. Jakob, “Large steps in inverse rendering of geometry,” *ACM Transactions on Graphics (Proceedings of SIGGRAPH Asia)*, vol. 40, no. 6, Dec. 2021. DOI: [10.1145/3478513.3480501](https://doi.org/10.1145/3478513.3480501).
- [33] M. D. Shuster, “Survey of attitude representations,” *Journal of the Astronautical Sciences*, vol. 41, no. 4, pp. 439–517, Oct. 1993.
- [34] B. Duvenhage, K. Bouatouch, and D. Kourie, “Numerical verification of bidirectional reflectance distribution functions for physical plausibility,” in *SAICSIT ’13: Proceedings of the South African Institute for Computer Scientists and Information Technologists Conference*, Oct. 2013, pp. 200–208, ISBN: 9781450321129. DOI: [10.1145/2513456.2513499](https://doi.org/10.1145/2513456.2513499).
- [35] D. Newell and E. Tiesinga, *The international system of units (si), 2019 edition*, en, Aug. 2019. DOI: <https://doi.org/10.6028/NIST.SP.330-2019>.
- [36] L. T. Sharpe, A. Stockman, W. Jagla, and H. Jägle, “A luminous efficiency function, $V^*(\lambda)$, for daylight adaptation,” *Journal of Vision*, vol. 5, no. 11, pp. 3–3, Dec. 2005, ISSN: 1534-7362. DOI: [10.1167/5.11.3](https://doi.org/10.1167/5.11.3). eprint: https://arvojournals.org/arvo/content/_public/journal/jov/932833/jov-5-11-3.pdf. [Online]. Available: <https://doi.org/10.1167/5.11.3>.
- [37] H. Krag, “A method for the validation of space debris models and for the analysis and planning of radar and optical surveys,” Ph.D. dissertation, Technische Universität Braunschweig, Mar. 2003.
- [38] C. Frueh, *Space traffic management*, Lecture Notes, 2019.

- [39] F. Falchi, P. Cinzano, D. Duriscoe, *et al.*, *Supplement to: The new world atlas of artificial night sky brightness. v. 1.1. gfz data services.* <https://doi.org/10.5880/GFZ.1.4.2016.001>, Accessed: 2023-08-25, 2016.
- [40] F. Falchi, P. Cinzano, D. Duriscoe, *et al.*, “The new world atlas of artificial night sky brightness,” *Science Advances*, vol. 2, no. 6, e1600377, 2016. DOI: [10.1126/sciadv.1600377](https://doi.org/10.1126/sciadv.1600377). eprint: <https://www.science.org/doi/pdf/10.1126/sciadv.1600377>. [Online]. Available: <https://www.science.org/doi/abs/10.1126/sciadv.1600377>.
- [41] F. Patat, O. S. Ugolnikov, and O. V. Postylyakov, “UBVRI twilight sky brightness at ESO-Paranal,” *Astronomy and Astrophysics*, vol. 455, no. 1, pp. 385–393, Aug. 2006. DOI: [10.1051/0004-6361:20064992](https://doi.org/10.1051/0004-6361:20064992). arXiv: [astro-ph/0604128 \[astro-ph\]](https://arxiv.org/abs/astro-ph/0604128).
- [42] A. e. a. Vallenari, “Gaia Data Release 3. Summary of the content and survey properties,” *Astronomy & Astrophysics*, vol. 674, A1, A1, Jun. 2023. DOI: [10.1051/0004-6361/202243940](https://doi.org/10.1051/0004-6361/202243940). arXiv: [2208.00211 \[astro-ph.GA\]](https://arxiv.org/abs/2208.00211).
- [43] J. C. Segovia, *Astroquery.gaia package*, <https://astroquery.readthedocs.io/en/latest/gaia/gaia.html>, Accessed: 2023-08-21, 2016.
- [44] G. M. Daniels, “A night sky model for satellite search systems.,” *Optical Engineering*, vol. 16, pp. 66–71, Feb. 1977.
- [45] F. E. Roach, “A Photometric Model of the Zodiacal Light,” *Astronomical Journal*, vol. 77, p. 887, Dec. 1972. DOI: [10.1086/111363](https://doi.org/10.1086/111363).